Tellus
SERIES A
DYNAMIC
METEOROLOGY
AND OCEANOGRAPHY
PUBLISHED BY THE INTERNATIONAL METEOROLOGICAL INSTITUTE IN STOCKHOLM

Tellus (2011), 63A, 4–23

The Rossby Centre Regional Climate model RCA3: model description and performance

By PATRICK SAMUELSSON*, COLIN G. JONES, ULRIKA WILLÉN, ANDERS ULLERSTIG, STEFAN GOLLVIK, ULF HANSSON, CHRISTER JANSSON, ERIK KJELLSTRÖM, GRIGORY NIKULIN and KLAUS WYSER, *Rossby Centre, SMHI, SE-601 76 Norrköping, Sweden*

(Manuscript received 14 February 2010; in final form 16 August 2010)

ABSTRACT

This paper describes the third full release of the Rossby Centre Regional Climate model (RCA3), with an emphasis on changes compared to earlier versions, in particular the introduction of a new tiled land-surface scheme. The model performance over Europe when driven at the boundaries by ERA40 reanalysis is discussed and systematic biases identified. This discussion is performed for key near-surface variables, such as temperature, precipitation, wind speed and snow amounts at both seasonal and daily timescales. An analysis of simulated clouds and surface turbulent and radiation fluxes is also made, to understand the causes of the identified biases. RCA3 shows equally good, or better, correspondence to observations than previous model versions at both analysed timescales. The primary model bias relates to an underestimate of the diurnal surface temperature range over Northern Europe, which maximizes in summer. This error is mainly linked to an overestimate of soil heat flux. It is shown that the introduction of an organic soil component reduces the error significantly. During the summer season, precipitation and surface evaporation are both overestimated over Northern Europe, whereas for most other regions and seasons precipitation and surface turbulent fluxes are well simulated.

1. Introduction

Regional Climate Models (RCMs) are now a widely accepted tool for downscaling Global Climate Models (GCMs), where they provide localized, high-resolution information, consistent with the large-scale climate simulated by the forcing GCM (e.g. Rummukainen, 2010, and references therein). As GCMs operate at a relatively coarse horizontal resolution, they do not resolve all regional details in surface heterogeneity. Therefore, dynamical downscaling of GCM simulations is of particular importance in regions of complex topography and large contrasts in surface features (e.g. land/water contrasts). Precipitation and near surface wind speeds are particularly sensitive to horizontal resolution due to their strong interaction with topography and surface physiography. Furthermore, key atmospheric processes, particularly those controlling the development of high-impact weather events, often interact across a range of spatial scales from the convective, through mesoscale to synoptic scales. The ability to capture this range of interactions and thereby provide useful information on extreme weather events improves with increasing model resolution. Hence the increased resolution of RCMs offers the potential for an improved simulation of the location, frequency and intensity of extreme events, such as localized precipitation and wind maxima. Possible changes in these rare, but high impact events are crucial to simulate in support of climate impact and adaptation projects.

In this paper, we describe the latest full release of the Rossby Centre Regional Climate model, RCA3, and document its performance for the recent climate over Europe. RCA3 is the version of the Rossby Centre Regional Climate Model that was frozen for all contributions to the ENSEMBLES project (van der Linden and Mitchell, 2009). Regional Climate projections from these ENSEMBLES runs and a number of other RCA3-based scenarios have been widely used in a range of climate impact studies over the past few years (see the examples listed in Jones et al., 2011, in this issue). Certain aspects of RCA3 and its performance have been published in numerous reports and papers. The purpose of this paper is to review the most important results of these publications and to put them into a common context together with some new explanations and discussions. We document the main physical parameterization changes in RCA3

*Corresponding author.
e-mail: patrick.samuelsson@smhi.se
DOI: 10.1111/j.1600-0870.2010.00478.x

compared to the previous full release, RCA2, as well as the main model biases for the present climate period when forced by the best available boundary conditions, namely ERA40 reanalyses (Uppala et al., 2005). A number of the biases reported in this paper have been investigated in the past 1–2 years. Some solutions on these biases will be briefly presented and discussed and they will also appear in the next RCA full release, RCA4, which is aimed for late 2010.

2. Description of RCA3

RCA is based upon the numerical weather prediction (NWP) model HIRLAM (Undén et al., 2002). Much of the initial work in the development of RCA was devoted to technical issues related to running a regional atmospheric model in a multiyear mode. From a physics perspective, perhaps the biggest difference between an NWP and a climate model is that the latter cannot rely on regular updates of the model's physical state from data assimilation. Thus, a climate model must be more consistent with respect to maintaining regional and global energy and water balances and in representing slower climate processes of lesser importance on NWP timescales.

RCA3 builds on the previous version RCA2 which is described in Jones et al. (2004).

One main concern with RCA2 was that the land surface parameterization, including sea ice, was fairly simplified (Bringfelt et al., 2001). For example, a single energy balance component with one surface temperature for an entire grid square was used. Thus, the representation of subgrid scale surfaces with very different properties, such as ice, snow, open land and forest, were characterized by the same surface temperature. Generally a tile approach, where a separate energy balance is used for each sub surface in a grid box, provides a better representation of important surface processes (Koster and Suarez, 1992). A tiled surface scheme was therefore introduced in RCA3 (Samuelsson et al., 2006). Grid boxes in RCA3 can now include fractions of sea (with fractional ice cover) or lake (with ice or not) and land. The land fraction can be further subdivided into forest and open land, where both can be partly snow covered. Each subgrid scale tile has a separate energy balance equation and individual prognostic surface temperatures. In RCA3, this is true for all surface temperatures, except for the sea-surface temperature (SST), which is prescribed from the boundary condition data set. In the coupled ocean–atmosphere version of RCA, RCAO (Döscher et al., 2009), SSTs are also prognostic.

The RCA3 dynamical core follows that in RCA2 and is a two time-level, semi-lagrangian, semi-implicit scheme with six-order horizontal diffusion applied to the prognostic variables. For more details, the reader is referred to Jones et al. (2004) and references therein. The RCA3 solution is relaxed towards the forcing boundary data across an eight point wide relaxation zone following the Davies' (1976) boundary formulation, with a cosine-based relaxation function.

In addition to the updated surface parameterization in RCA3, compared to RCA2, a number of changes have also been made in the radiation, turbulence and cloud parameterizations. All these changes are described in Sections 2.1 and 2.2.

2.1. The surface scheme

The land-surface scheme (LSS) in RCA3 (Fig. 1) belongs to the second generation of LSSs (Sellers et al., 1997) which means that it has fairly advanced treatments of many physical land-surface processes but it does not account for carbon dioxide (CO_2)

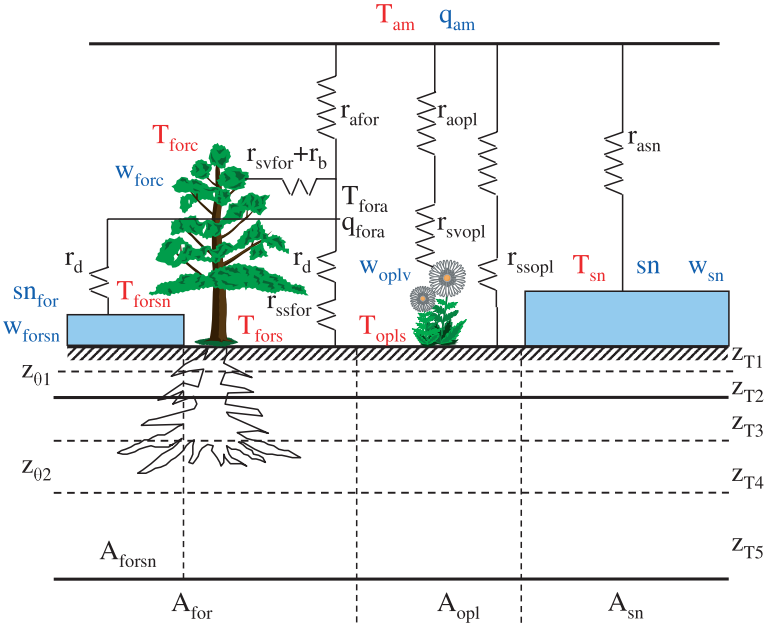

Fig. 1. A principal sketch of the land-surface scheme in RCA3. Fractions of individual tiles are denoted by A_{xx}. Prognostic temperatures are marked in red and prognostic water and humidity variables in blue. Subscripts 'am' refer to the atmospheric lowest model level. The diagnostic canopy air temperature and specific humidity, T_{fora} and q_{fora}, are marked in black. Aerodynamic and surface resistances are denoted by r_{xx}. Vertical layers in the soil are indicated by z_{T1}–z_{T5} with respect to temperature and by $z_{\theta 1}$ and $z_{\theta 2}$ with respect to soil water, respectively. The sub-boxes in the soil are divided by solid and dashed lines. For further details please refer to the text.

effects on canopy conductance in evapotranspiration calculations. In RCA2, the evapotranspiration is parameterized according to Noilhan and Planton (1989), which follows the 'big leaf' concept by Deardorff (1978) in which no distinction is made between soil and canopy. However, Wallace et al. (1990) showed that the interactions between the fluxes from the soil and the canopy can be significant in sparse canopies, especially for very wet or very dry soil conditions. In the development of RCA3 it was anticipated that such rare conditions are most relevant for forest processes. In addition, from the atmospheric point of view, the forest canopy represents a surface which reacts quickly to changes in energy fluxes due to its low heat capacity. Therefore, the forest subtile ($A_{\rm for}$ in Fig. 1) was parameterized according to the double-energy balance concept (Shuttleworth and Wallace, 1985) which means that the forest canopy ($T_{\rm forc}$) and the forest floor have separate energy balances and separate prognostic temperatures. In RCA3, we also separate the forest floor into a bare soil ($T_{\rm fors}$) and a snow covered part ($T_{\rm forsn}$), respectively. The parameterization of the double-energy balance in the forest follows Choudhury and Monteith (1988), which includes the formulation of the aerodynamic resistances $r_{\rm b}$ and $r_{\rm d}$. The canopy air temperature, $T_{\rm fora}$, and specific humidity, $q_{\rm fora}$, are diagnostic quantities which are solved by assuming conservation of fluxes.

The prognostic snow storages over open land, *sn*, and in the forest, $sn_{\rm for}$, are parameterized using a bulk one-layer concept where the top most 15 cm of the snow pack is assumed to be thermally active, characterized by its prognostic snow temperature, $T_{\rm sn}$ and $T_{\rm forsn}$, respectively. The temperature below that layer is in principle unknown which means that the snow-soil heat transfer must be parameterized. The snow can hold 10% of its snow water equivalent as liquid water, $w_{\rm sn}$ and $w_{\rm forsn}$, respectively. The sources of liquid water are snow melt water and rain that falls on 0°C snow. The prognostic snow density, $\rho_{\rm sn}$ and $\rho_{\rm snfor}$, is set to 100 kg m^{-3} for fresh snow and increases with time as the snow ages (Douville et al., 1995). The freezing of any liquid water in the snow contributes to an increase of the density using the density of ice. The snow fraction, $A_{\rm sn}$ and $A_{\rm forsn}$, is calculated following Lindström and Gardelin (1999). They showed that, according to observations, the snow cover for a deep snow pack is better correlated with the ratio $sn/sn_{\rm max}$ than with *sn* itself, where $sn_{\rm max}$ is the maximum snow water equivalent reached during the snow season. During snow melt, the snow fraction is not allowed to decrease before sn reaches a certain fraction of $sn_{\rm max}$. This fraction is set to 0.6 for flat terrain but increases with increased subgrid orography. For open-land snow there is a prognostic snow albedo, allowed to be in the range 0.6–0.85, based on the method described by Douville et al. (1995) which simply makes the albedo decrease with time as snow is ageing. The ageing is faster for melting than for non-melting snow. For snow in forest the albedo is set constant to 0.20.

The open-land subtile, $A_{\rm opl}$, consists of a vegetated part and a bare-soil part, both characterized by the same prognostic temperature, $T_{\rm opls}$. The surface resistance for the evapotranspiration, $r_{\rm soplv}$, follows Jarvis (1976) and the soil-surface resistance, $r_{\rm sopls}$, follows van den Hurk et al. (2000). Interception of rain, $w_{\rm forc}$ for the forest and $w_{\rm oplv}$ for open-land vegetation, is parameterized according to Noilhan and Planton (1989).

The aerodynamic resistances in the surface layer, $r_{\rm ax}$, are based on the parameterization of near-surface fluxes of momentum and scalar quantities according to Louis et al. (1982), where individual roughness lengths and stability corrections are used for each subtile. The individual fluxes of heat and momentum from these tiles are weighted to grid-averaged values at the lowest atmospheric model level according to the fractional areas of the tiles.

The soil is divided into five layers with respect to temperature with a no-flux boundary condition at 3.0 m depth. The thicknesses of the layers increase from 1.0 cm for the top-most layer to 1.89 m for the deepest layer. There are separate soil columns below the forest and open-land tiles ($A_{\rm for}$ and $A_{\rm opl}$) and additional soil columns appear when snow is present ($A_{\rm forsn}$ and $A_{\rm sn}$). To fulfil the energy balance, heat energy is moved between the snow and non-snow covered soil columns as the snow fraction changes. There are seven different texture classes based on the geographical distribution of soil types FAO-UNESCO (1981) digitized for Europe by the German Weather Service. The heat diffusivity equations follow McCumber and Pielke (1981) and the soil properties Clapp and Hornberger (1978).

For soil water there are two layers, 0.07 and 2.20 m thick, except for in mountain areas where the deep layer is 1.00 m (altitude $>$600 m and deep soil climatology temperature $<$7°C). The vertical transport of water is expressed using Richards equation (Hillel, 1980) but the hydraulic conductivity term is replaced by a drainage/runoff parameterization, the β-formulation, as used in the hydrological model HBV (Lindström et al., 1997). The LSS does not include phase changes between liquid water and ice in the soil but instead we parameterize the effect that soil ice would have had on soil heat capacity (Viterbo et al., 1999) and on root extraction of water.

The snow-free land-surface albedo is set to 0.15 for the forest (canopy and forest floor) and to 0.28 for open land. As will be discussed later, the open-land value is high compared to observed values which are around 0.18. The leaf-area index (LAI) is calculated as a function of the soil temperature in layer four (Hagemann et al., 1999) with lower limit set to 0.4 and upper limits set to 2.3 and 4.0 for open land and deciduous forest, respectively. If deep soil moisture reaches the wilting point the LAI is set to its lower limit. LAI for conifers forest is set constant to 4.0.

The land-sea mask is provided from HIRLAM climate fields (Källén, 1996) and the forest fraction is given by Hagemann et al. (1999). However, the more recent physiography data base ECOCLIMAP (Masson et al., 2003) gives generally less fraction of forest than the Hagemann forest fraction. To reach better correspondence with the ECOCLIMAP physiography, the final

forest fraction in RCA3 was reduced to 80% of its original value.

Lakes in RCA3 are simulated with the multilayer lake model PROBE (Ljungemyr et al., 1996). PROBE is forced from RCA3 by 2 m air temperature and humidity, 10 m wind speed and downward short-wave (SW) and long-wave (LW) radiation. It simulates water temperature at different levels and the growth of ice. Depth of lakes are given for Swedish lakes but set to 10 m for all lakes outside Sweden. Water surface temperature and ice thickness is provided to RCA which uses these to calculate fluxes of momentum and heat.

The temperature of sea and lake ice is simulated by the heat-transfer equation for an ice cover with two layers assuming constant ice thickness for sea (0.5 m in the Baltic Sea and 1 m for the rest of the ocean) and ice thickness given by PROBE for lakes. Ice albedo is set to 0.5. The heat flux at the ice–water interface is parameterized assuming a constant melting temperature of the ice at the bottom. Snow on ice is simulated as over land but with the prognostic snow albedo limited to the range 0.7–0.85.

Diagnostic variables of temperature and humidity at 2 m and wind at 10 m are calculated using Monin–Obukhov similarity theory. These diagnostic variables are first calculated individually for each tile and then area-averaged for larger subsurfaces or for the whole grid square. When evaluating the RCA diagnostic 2 m air temperature, T2m, against observations we chose to use the simulated T2m over open land fractions of a grid box, $T2m_{opl}$ (snow and snow-free area average), because observational stations generally report temperatures in open land areas or in glades in forest areas. The forest T2m, $T2m_{for}$, is defined as the air temperature at 2 m height above the forest floor. As both radiation fluxes and turbulent fluxes at the forest floor are greatly reduced due to the presence of the overlaying canopy $T2m_{for}$ variability will be much lower than any nearby $T2m_{opl}$ variability. The grid-averaged T2m, $T2m_{grid}$, is simply an area weighted average of the individual tiles, sea (water and/or ice), lake (water or ice), forest and open land.

For the Baltic Sea drainage basin the runoff from each grid square can be routed to form river discharge for certain rivers along the Batic Sea coast. This routing is based on the hydrological HBV model and it is specifically calibrated for the Baltic basin (Graham, 2002).

For a more detailed description of the LSS in RCA3 please refer to Samuelsson et al. (2006).

2.2. *Changes in the atmospheric parameterization schemes*

The radiation scheme in RCA3 is based on the HIRLAM radiation scheme, originally developed for NWP purposes (Savijärvi, 1990; Sass et al., 1994). The scheme is computationally extremely fast but also highly simplified, with only one wavelength band for LW radiation and one for SW. The scheme was modified to include CO_2 absorption and an improved treatment of the water vapour continuum by Räisänen et al. (2000). In RCA2, the SW cloud albedo and LW cloud emissivity were calculated from the cloud water content, with a cloud mass absorption coefficient depending only on altitude. In RCA3, cloud emissivity and cloud albedo are now formally linked to cloud liquid water and ice amounts, with a diagnostic calculation of effective radius performed separately for liquid and ice (Wyser et al., 1999). In the radiation scheme, the grid box mean liquid water path is multiplied by a scaling factor of 0.7 before cloud albedo and emissivity are calculated. This is done to account for the fact the RCA radiation code, like the majority of radiation schemes, assumes cloud water to be homogeneously distributed throughout a given grid box cloud fraction, the so-called plane-parallel approximation. As discussed in Barker and Wielicki (1997), Barker (1996), Tiedtke (1996) and Cahalan et al. (1994), use of the plane-parallel approximation will always bias cloud albedo to be higher than equivalent real clouds. In real clouds within-cloud small-scale variability in the cloud-water distribution, with small areas of ascent exhibiting very high cloud water amounts and regions of weaker ascent or even descent having much lower cloud water amounts, leads to an average cloud albedo significantly lower than if the same amount of cloud water were distributed in a plane-parallel sense. Barker et al. (1996) and Barker and Wielicki (1997) discuss more advanced methods for deriving a suitable scaling factor to account for this systematic discrepancy. Such advanced treatment has so far not been tested in RCA.

RCA3 carries a single prognostic equation for the total cloud water mixing ratio, separation into liquid and ice components is diagnosed as a function of local air temperature. In RCA3, this calculation has been modified, compared to RCA2, so that water is now more rapidly put into the ice phase as a function of decreasing temperature. As a result, for a given (cold) cloud, emissivity is reduced in RCA3 relative to RCA2, with a commensurate reduction in downwelling LW radiation. In both the radiation and cloud microphysical schemes, droplet effective radii are based on a prescribed cloud droplet number concentration (CDNC) which is allowed to vary as a function of surface type (land, sea, snow-covered land, ice-covered water). Over land CDNC varies as a linear function of height, decreasing with pressure from a typical surface land value (400 cm^{-3}) to a typical oceanic and free atmospheric value (150 cm^{-3}) at 0.8 times the surface pressure.

To reduce an overestimate of clear-sky SW surface fluxes found in RCA2, in RCA3 the clear-sky water-vapour absorption of SW was modified and the clear-sky SW absorption by aerosols increased. In the RCA2 radiation scheme, emission of LW radiation to the surface from the cloudy fraction of a model grid column occurs from the base of the lowest cloud layer, with the cloud water and cloud fraction treated in a vertically integrated, maximum overlap manner (Sass et al., 1994). The amount of LW radiation emitted from the cloud-base that actually reaches

the surface is then scaled by the emissivity of the clear-sky atmosphere below cloud base and normalized by the vertically integrated cloud fraction. Clear-sky LW radiation reaching the surface is considered as an average of the entire vertical atmospheric column emission and assumed to operate over the entire model grid box (i.e. over both clear and cloudy fractions of a grid box). In RCA3, the LW emission is now more formally split into three fractional regions of a given grid box vertical column. The cloud-fraction emission is treated as in RCA2, but now the clear sky emission is separated into two contributions. The first is an assumed emission/absorption process which considers the entire vertical column and is normalized by the clear-sky fraction of the column. The second clear-sky contribution comes from the emission of clear-sky LW radiation below the fractional cloud base, where the clear-sky emissivity is based on the thermodynamic profile below cloud base only. The resulting LW flux is then normalized to cover only the cloudy-part of the grid box. These three contributions, all weighted by their respective cloudy or clear-sky fraction, are then combined into a single, grid-box mean LW flux to the surface.

In RCA2, the turbulence parameterization was a dry prognostic turbulent kinetic energy (TKE) scheme, combined with a diagnostic mixing length (Cuxart et al., 2000). The scheme is updated in RCA3 to include moist processes in the calculation of TKE (Cuijpers and Duynkerke, 1993) and to have a smoother transition between stable and unstable conditions (Lenderink and de Rooy, 2000; Lenderink and Holtslag, 2004). The new scheme has the same basic philosophy as in RCA2, but uses a simpler and faster method to calculate turbulent mixing lengths and better matches these to near surface lengths given by similarity theory in the neutral limit. Furthermore, the new scheme employs an implicit treatment of the TKE equation (Brinkop and Roeckner, 1995) making it numerically more stable.

Moist processes in RCA2 and RCA3 are separated into resolved (large-scale) clouds and subgrid scale (convective) clouds. Large-scale clouds are described using the scheme of Rasch and Kristjánsson (1998). Convective processes are described with an entraining and detraining plume model using the approach of Kain and Fritsch (1990, 1993) and Kain (2004).

The treatment of shallow convective clouds, condensate and precipitation has been substantially modified in RCA3 compared to RCA2. The main change is that in RCA3 the Kain–Fritsch convection scheme now assumes that shallow convection is non-precipitating. Shallow convective cloud water produced by the Kain–Fritsch convection is instead detrained into the environment and a fraction evaporated depending linearly on the local grid box mean relative humidity. The remaining shallow convective cloud water is assumed to reside in a diagnosed shallow cumulus cloud fraction that links cloud amount to the liquid and vapour content of the convective plumes and the local relative humidity (Albrecht, 1981). Microphysical conversion of shallow convective cloud water to precipitation is then performed by the same scheme as for large-scale condensation. The resulting shallow cumulus clouds and cloud water can then interact with the radiation fields. The main impact of these changes is reduced precipitation from shallow convective clouds, a formal shallow convective cloud fraction (not present in RCA2) and thus shallow convective clouds that contain more water, are more reflective and can interact with atmospheric radiation fluxes. A more detailed description of the new parameterization is given in Jones and Sanchez (2002).

In the formulation of large-scale precipitation some minor modifications have been made to the liquid autoconversion calculation in RCA3. These act to reduce the occurrence of weak precipitation, which was too frequent in RCA2. As mentioned earlier, the diagnostic separation of total cloud water into liquid and ice was modified in the RCA3 radiation scheme. This modification was also carried out in the cloud microphysical scheme to maintain consistency through the model.

3. Model setup and evaluation data

3.1. Model setup

RCA3 was setup on a rotated latitude–longitude grid over Europe with a resolution of 0.44°, corresponding to ∼50 km. The land-sea mask, the fractions of lakes and forests, and the orography are shown in Fig. 2. The domain includes 102 × 111 grid boxes of which the outermost eight on each side are used as boundary relaxation zones. The relaxation zone is excluded in all figures shown. In the vertical, 24 unequally spaced hybrid terrain-following levels are used (Simmons and Burridge, 1981). The time step was 30 min.

Our analysis is based on an experiment covering the time period January 1961–December 2001. Prior to this period, a 4-month spinup is performed which is initialized by ERA40. The lateral boundary fields and SST forcing are taken from ERA40 every 6 h, with linear time interpolation in between. The solar constant is prescribed as 1370 Wm^{-2}. In terms of greenhouse gas forcing, we have imposed a linear increase with time of equivalent CO_2 identical to that used for producing the ERA40 data set (1.5 ppm_v per year).

3.2. Evaluation data

Results from the RCA3 simulations are compared to a number of observational data sets listed in Table 1. When we lack information on gridded observations for a particular variable we have used ERA40 for comparison. In those cases when there are indications that ERA40 itself is biased compared to observations we take note of that in the discussion of model accuracy and bias. Some differences do exist between the two versions of E-OBS (Table 1) due to changes in applied time series of observations and in the processing of data. Because these differences are most evident in the probability density functions of precipitation we

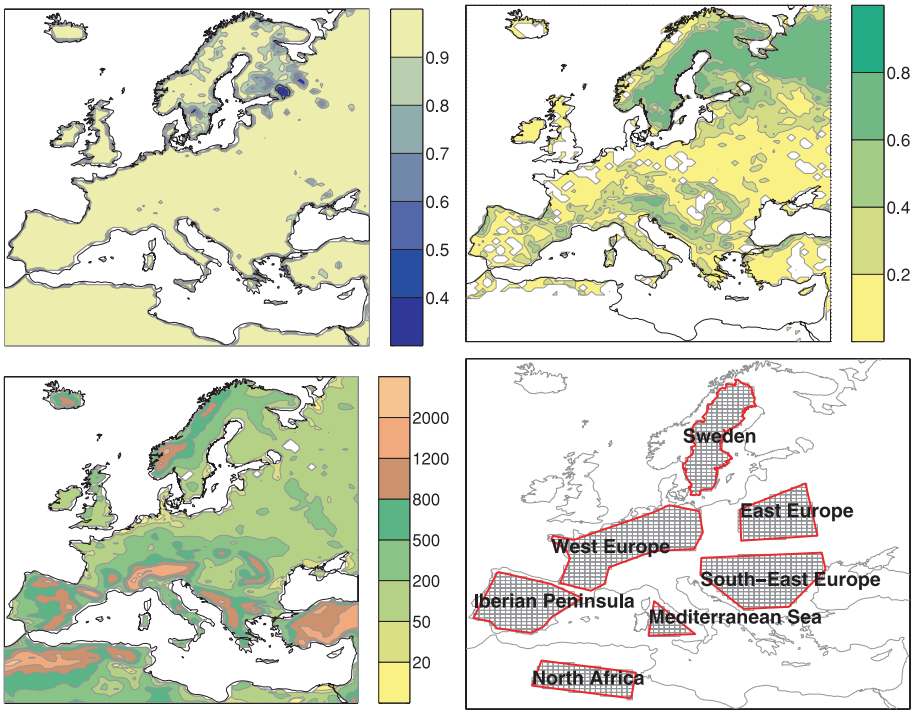

Fig. 2. Top panel: Land fraction with coastal regions and lakes shown in blue colours (left) and forest fraction (right). Bottom panel: Orography in metres (left) and regions as used for presentations of results (right).

Table 1. Data sets that have been used for model evaluation in this report

			Resolution		
Dataset	Description	Variables	Time	Space	Reference
CRU	Climate Research Unit version TS 2.1	T2m[a], precipitation, cloud cover	Monthly	0.5°	Mitchell and Jones (2005)
E-OBS1	European gridded observations, version 1.1	T2m (mean, max, min) and precipitation	Daily	0.44°	Haylock et al. (2008)
E-OBS2	European gridded observations, version 2.0	T2m (mean, max, min) and precipitation	Daily	0.44°	http://eca.knmi.nl/download/ensembles/download.php
Willmott	Version 3.02	T2m[a], precipitation	Monthly	0.5°	Willmott and Matsura (1995)
ERA40	European Centre for Medium range Weather Forecasts (ECMWF) 40 years reanalysis	T2m[a], precipitation, SLP, wind speed	Monthly	1.0°	Uppala et al. (2005)

[a]As a first-order correction these climatologies have been adjusted for differences in elevation compared to the RCA grid by using a lapse rate of $-0.0065\ \mathrm{K\,m^{-1}}$.

include both versions for the comparison with RCA3 in that case.

4. Results

In this paper we evaluate near-surface variables, for example 2 m air temperature, precipitation and snow cover on monthly and daily timescales. We also evaluate the distribution functions of both quantities in terms of maximum and minimum values and the diurnal range (temperature) and intensity distributions (precipitation). Near-surface wind speed is a parameter of interest to users. However, due to observational limitations, near-surface wind speeds are only briefly discussed in this study. He et al. (2010) have performed a detailed analysis of RCA3 winds over North America and readers are referred to this paper for more details. Where systematic biases are detected in one of these key variables, further analysis is performed of other simulated fields that may contribute to these biases (e.g. radiation fluxes, surface

turbulent fluxes and cloud cover). To provide an overview of the simulated circulation features in RCA3, we begin our evaluation with mean sea-level pressure.

Results are presented in maps or as area averages for the regions defined in Fig. 2. We especially concentrate on Sweden and the Iberian Peninsula as examples of two different climate regimes. The definition of the seasons referred to are: winter (December, January, February), spring (March, April, May), summer (June, July, August) and autumn (September, October, November). The empirical probability distribution functions (PDFs) shown are based on daily mean values spatially averaged over regions. Many of the maps and annual cycle plots can be found in earlier publications but all PDFs have been prepared for this specific paper and have not been published before.

4.1. Mean sea-level pressure

Figure 3 presents the seasonal mean difference in mean sea level pressure (MSLP) between RCA3 and the forcing ERA40. These differences are relatively small, indicating that RCA3 reproduces the large-scale circulation of the ERA40 boundary conditions. There are, however, some noteworthy differences. In the Mediterranean region, MSLP is higher in RCA3 than in ERA40 in all seasons, particularly in autumn and winter, with a reverse, negative MSLP anomaly east of the Alps in winter. These features are largely unchanged from RCA2 and were also noted in Jones et al. (2004). They speculated that RCA2 may not represent lee cyclogenesis downstream of the Alps and the Pyrenees properly. Possible contributory factors are being investigated, including the role of orography and the parameterization of subgrid scale orographic momentum drag, both of which are known to influence synoptic development (Milton and Wilson, 1996; Smith et al., 2006).

Figure 3 also compares PDFs of MSLP for Sweden, the Iberian Peninsula and a third region centred on the Mediterranean Sea. PDFs are presented for all four seasons from RCA3 and ERA40. Over Sweden and Iberia, all PDFs indicate that RCA3 captures both the median synoptic activity well and the width of the distribution (i.e. the magnitude of daily to seasonal synoptic variability). Over Iberia there is a tendency for the RCA3 PDF to be slightly shifted towards higher pressures. This is particularly the case at the higher end of the SLP distribution, where generally anti-cyclonic conditions occur, suggesting the

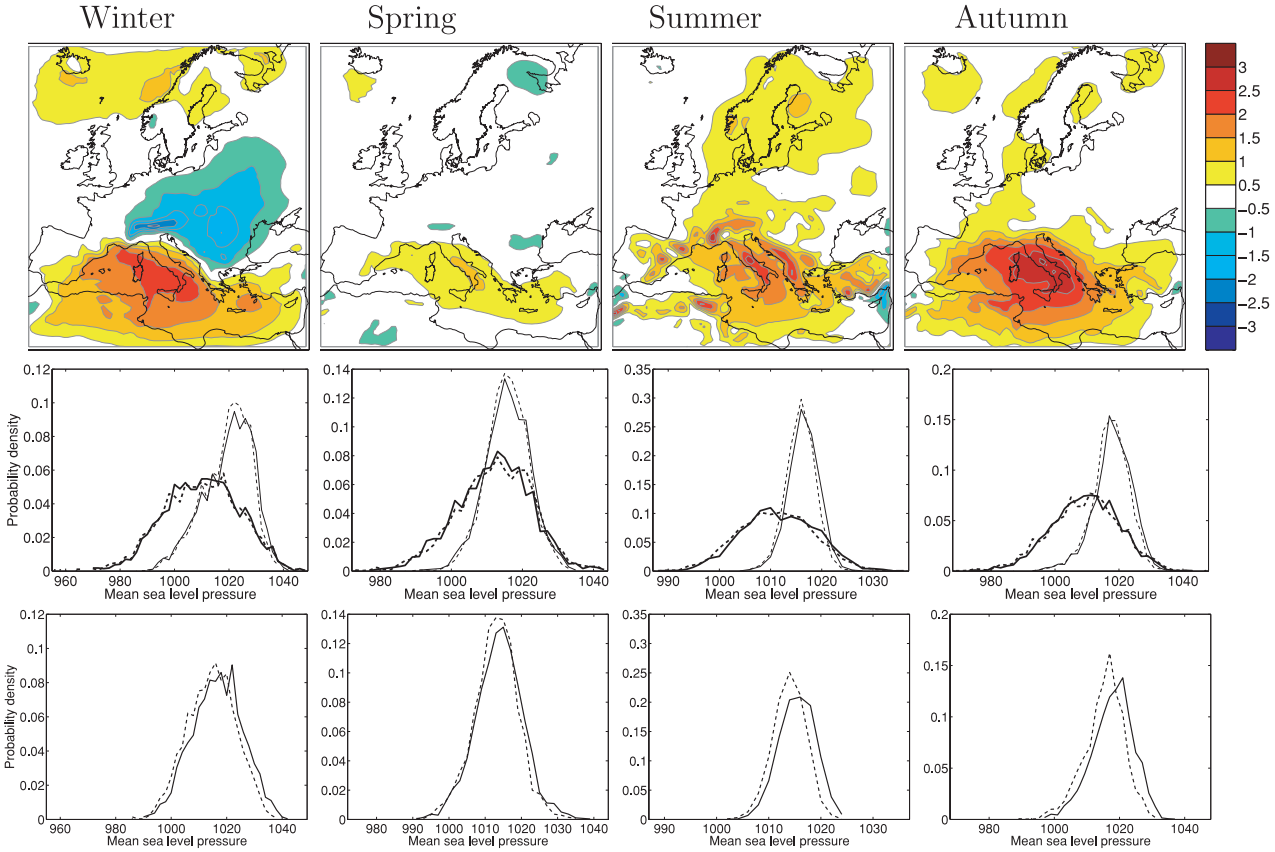

Fig. 3. Top panel: Difference in MSLP (hPa) between RCA3 and ERA40. Middle panel: Probability density functions of daily mean MSLP (hPa) for RCA3 (solid) and ERA40 (dashed) for Sweden (thick) and the Iberian Peninsula (thin). Bottom panel: As middle panels but for the Mediterranean Sea. The columns represent the four seasons winter, spring, summer and autumn.

positive pressure bias seen in the seasonal mean figures may actually arise from an overestimate in the intensity and frequency of anti-cyclonic conditions. This tendency is even more pronounced in the Mediterranean PDFs.

Kjellström et al. (2005) evaluated the interannual variability of SLP, based on monthly mean values as simulated by RCA3, and found this to be in good agreement with ERA40. This agreement is best during winter and worse in summer, consistent with a stronger forcing from the lateral boundaries in winter (Lucas-Picher et al., 2008).

4.2. Two meter air temperature

4.2.1. Mean climate. In general, the simulated 2 m air temperature over open land, $T2m_{opl}$, is within $\pm 1^{\circ}$C on a seasonal basis when compared to a mean value of observations based on CRU, Willmott and E-OBS2. There are, however, two major exceptions, both during autumn and winter (Fig. 4); a warm bias in the northeastern part of the model domain and a cold bias in Southern Europe and North Africa. In these areas localized biases of up to 3–4°C can occur. Biases in the northeastern part of the domain are particularly pronounced in winter. The wintertime bias in Northern Scandinavia may partly be an artefact of observation sampling, with observations often taken in valleys that tend to be colder than their surroundings during stable and cold conditions in winter (Räisänen et al., 2003). However, the warm winter bias in North West Russia is likely primarily due to an underestimate of snow (see Section 4.6 and Fig. 10) as snow acts to insulate the surface and reduce near-surface turbulence. Recent studies have shown that RCA3 underestimates snow albedo in cold climate regions which are dominated by low intensities in snow fall. Due to feedback mechanisms such an underestimation leads to warmer air temperature and less snow accumulation.

Causes for the winter-autumn cold bias over the Mediterranean region are less clear. The winter season temperature PDFs over Iberia clearly indicate a bias in RCA3 towards too frequent cold days. Such an error structure is consistent with an overestimate in the intensity and/or frequency of winter anti-cyclonic conditions, indicated for this region from the MSLP PDFs in Fig. 3. Winter anti-cyclonic circulation will generally be associated with dry, clear-sky conditions and therefore relatively strong LW cooling.

The interannual variability of RCA3 near-surface temperature was also analysed by Kjellström et al. (2005). The temporal correlation in monthly mean anomalies between CRU and RCA3 being $\sim$0.95 in winter over Sweden, decreasing to $\sim$0.9 in summer. Interannual variability of the near-surface temperatures generally lies with in $\pm$20% of observations

4.2.2. Diurnal cycle and extreme temperatures. For Sweden, the PDFs of simulated $T2m_{opl}$ are generally somewhat narrower than the corresponding PDFs for observations (Fig. 4). On the cold side of the distribution, RCA is somewhat too warm while the warm tail of the distribution is well captured, except for an underestimate of very warm days (diurnal mean temperature $>17^{\circ}$C) in summer. Over Iberia the simulated and observed PDFs are quite similar in their shape, although the RCA PDFs are shifted towards a cold bias except in spring. In winter, the shift is largest on the cold side of the distribution as discussed in Section 4.2.1. These findings are consistent with those of Kjellström et al. (2007) who, based on a wide range of RCMs, concluded that the biases in RCMs are usually larger in the 95th/5th percentiles than the corresponding biases in the median, that is the biases generally increase towards the tails of the probability distributions.

The diurnal temperature range for RCA3 and observations are shown in Fig. 5. The spatial map shows an 11-year mean, summer season diurnal range, whereas the curves show the mean annual cycle of the diurnal range, spatially averaged for the two selected regions Sweden and the Iberian Peninsula. The mean diurnal temperature range is calculated as the average difference between the daily maximum and minimum temperatures. For RCA3, $T2m_{opl}$ values are used. In general, the observations have a larger diurnal range than the model. This is particularly true over Northern Europe where the observed diurnal temperature range can be up to 5°C greater than the simulated. The causes of this discrepancy are at least two: (i) The LSS in RCA3 assumes only mineral soils across Europe, which causes the ground heat flux to be overestimated. (ii) There is an excess of cloud water in RCA3 (see Fig. 8 and Section 4.4), leading to an overestimate of both cloud emissivity and cloud albedo. The former contributes to a positive bias in downwelling LW at the surface, limiting nocturnal cooling, whereas the latter causes a negative bias in downwelling SW at the surface, reducing day time maximum temperatures. LW emissivity rapidly saturates to unity at low cloud water amounts, whereas SW cloud albedo varies over a much wider range of cloud water values (Stephens and Webster, 1979; Slingo and Schrecker, 1982). This difference in sensitivity results in the positive bias in cloud water impacting more strongly and more frequently cloud SW albedo than LW emissivity. This, along with the increasingly large absolute flux of SW during the day, peaking at local noon, result in the cloud albedo effect on SW surface fluxes being the leading term driving temperature errors across the diurnal cycle. The net effect of such a skewed cloud-radiation error is larger negative biases in the maximum (day time) 2 m temperatures than the corresponding positive bias in minimum (nocturnal) temperatures (Fig. 4). Further analysis of the simulated cloud and radiation fields are presented in Section 4.4. Over Iberia the diurnal range is close to observations in summer, with some error cancellation across the diurnal cycle (an underestimate in the maximum temperatures being partly offset, in terms of the diurnal range, by an overestimated, too cold, minimum temperature). During all other seasons the diurnal cycle over Iberia is underestimated by $\sim$1–2°C and mainly results from maximum temperatures being too low.

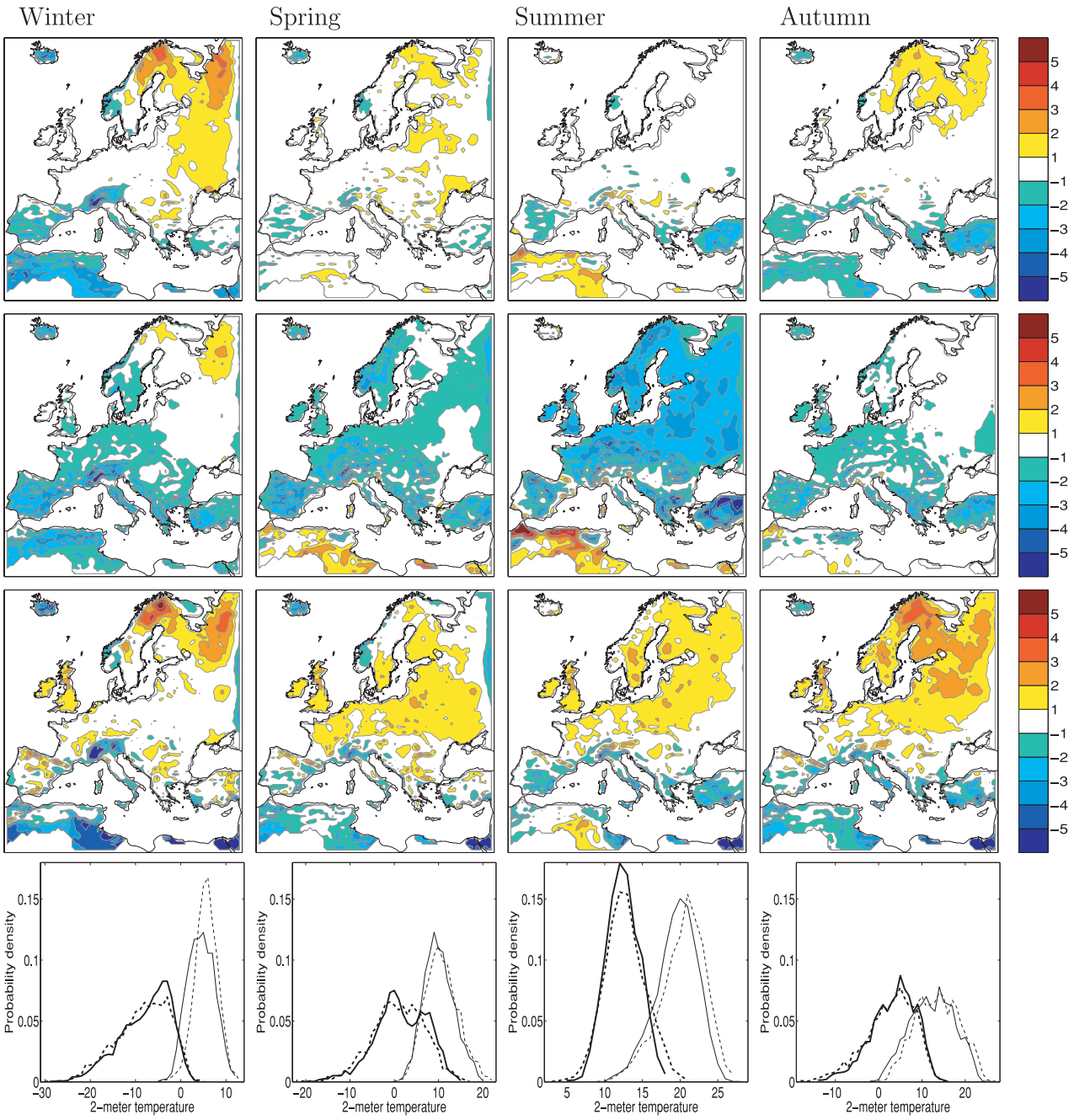

Fig. 4. Maps top panel: Seasonal mean difference (°C) in T2mopl between RCA3 and a mean value of observations based on CRU, Willmott and E-OBS2. Maps middle panel: Seasonal mean difference (°C) in daily maximum $T2m_{opl}$ between RCA3 and E-OBS2. Maps bottom panel: As panels above but for daily minimum $T2m_{opl}$. PDF panel: Probability density functions of daily mean $T2m_{opl}$ (°C) for RCA3 (solid) and E-OBS2 (dashed) for Sweden (thick) and the Iberian Peninsula (thin). The columns represent the four seasons winter, spring, summer and autumn.

As the underestimation of the diurnal cycle of $T2m_{opl}$ has been identified as one of the major shortcomings in the performance of RCA3 we would like to briefly present how new development in RCA4 has contributed to decrease this underestimation. Figure 5 shows that the RCA4 diurnal temperature range has increased significantly. Over Sweden the summer underestimation has been reduced from 4.5 to 2°C. The main contributing factor to this improvement is a reduction of the overestimated ground heat flux. Lawrence and Slater (2008) have shown that soils at high latitudes have a larger organic component. Because organic soil has lower heat transfer coefficient than mineral soil the introduction of organic carbon as a fractional component

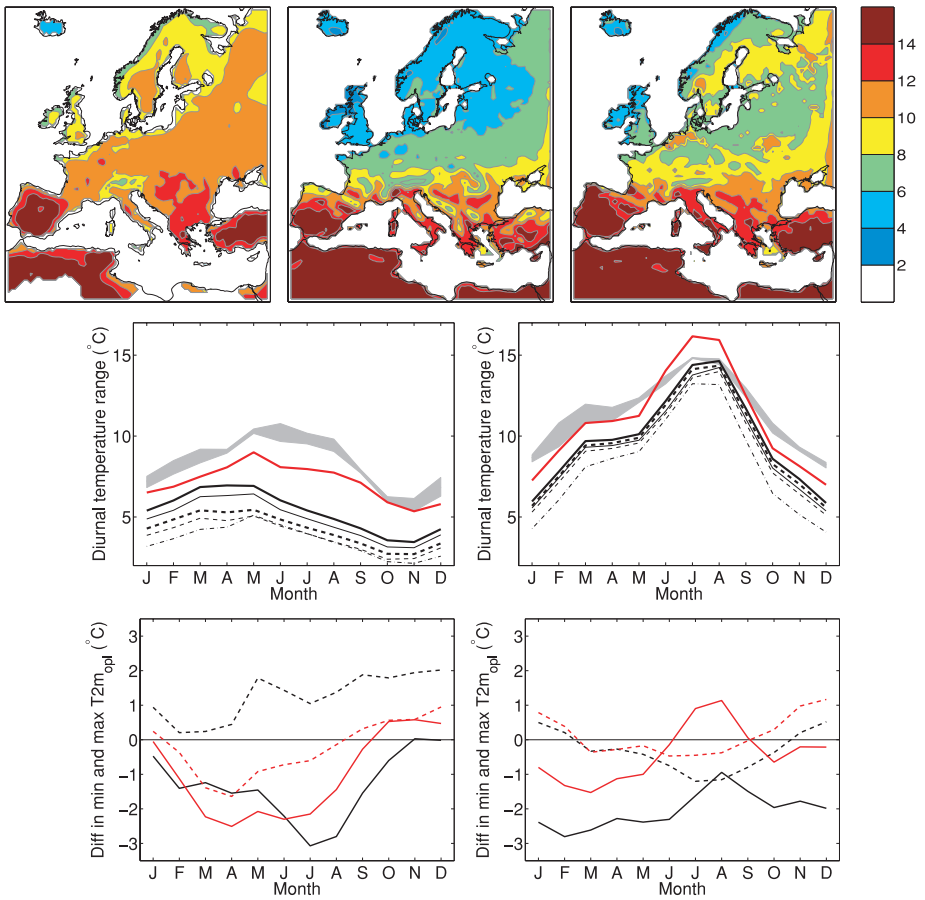

Fig. 5. Top panel: Eleven-year (1990–2001) summer mean diurnal temperature range (°C) for a mean value of CRU and E-OBS2 (left), RCA3 ($T2m_{opl}$, middle) and for RCA4 ($T2m_{opl}$, right). Middle panel: Area averaged annual cycles of the diurnal temperature range for Sweden (left) and the Iberian Peninsula (right). The black lines are for RCA3 results where the thick line types represent daily max—daily min of $T2m_{opl}$ (full) and $T2m_{grid}$ (dashed). A diurnal range based on 3 hourly model output is represented by thin lines for $T2m_{opl}$ (full), $T2m_{grid}$ (dashed) and $T2m_{for}$ (dash-dotted), respectively. The red lines are for RCA4 results representing daily max − daily min of $T2m_{opl}$. The shaded area includes observations based on CRU and E-OBS2. Bottom panel: Area averaged seasonal cycles of differences RCA-E-OBS2 for daily maximum (solid) and minimum (dashed) $T2m_{opl}$. The black and red lines represent RCA3 and RCA4, respectively.

of the prescribed soil characteristics in RCA4 reduced the heat transfer in the soil which led to increased diurnal cycle. As seen from Fig. 5, this increase originates mainly from a reduction of the bias in the minimum temperature and to a lesser extent from a reduction of the bias in the maximum temperature. Over the Iberian Peninsula the amount of carbon in the soil is less than over Sweden. However, the impact of carbon soil is still seen, here as an increase in the maximum temperature.

From the annual cycles of the diurnal temperature range (Fig. 5), it is clear that a diurnal cycle based on the difference between maximum and minimum daily temperatures is larger than one based on less frequent output (e.g. 3-hourly data). For RCA3 it can also be seen that the open-land diurnal range is larger than the diurnal range based solely on the forest fraction of equivalent grid boxes. For regions where grid boxes contain a significant fraction of forest, such as Sweden, the simulated diurnal temperature range can be as much as 1.5°C less based on the grid box average temperature than the open-land fraction of the same grid boxes. Furthermore, in such forest dominated landscapes, the 3-hourly open-land temperatures give a larger diurnal range than the difference between maximum and minimum daily grid-averaged temperatures.

4.3. Precipitation

Figure 6 shows the geographical distribution of seasonal mean precipitation in RCA3, compared to ERA40 and a combined observation data set. Figure 7 shows the same data plotted as spatially averaged annual cycles for the six regions outlined in Fig. 2. The higher resolution in RCA3 compared to the ERA40 is clearly seen in some areas like the Atlantic coast of Norway. Here, RCA3 shows more precipitation over land than ERA40

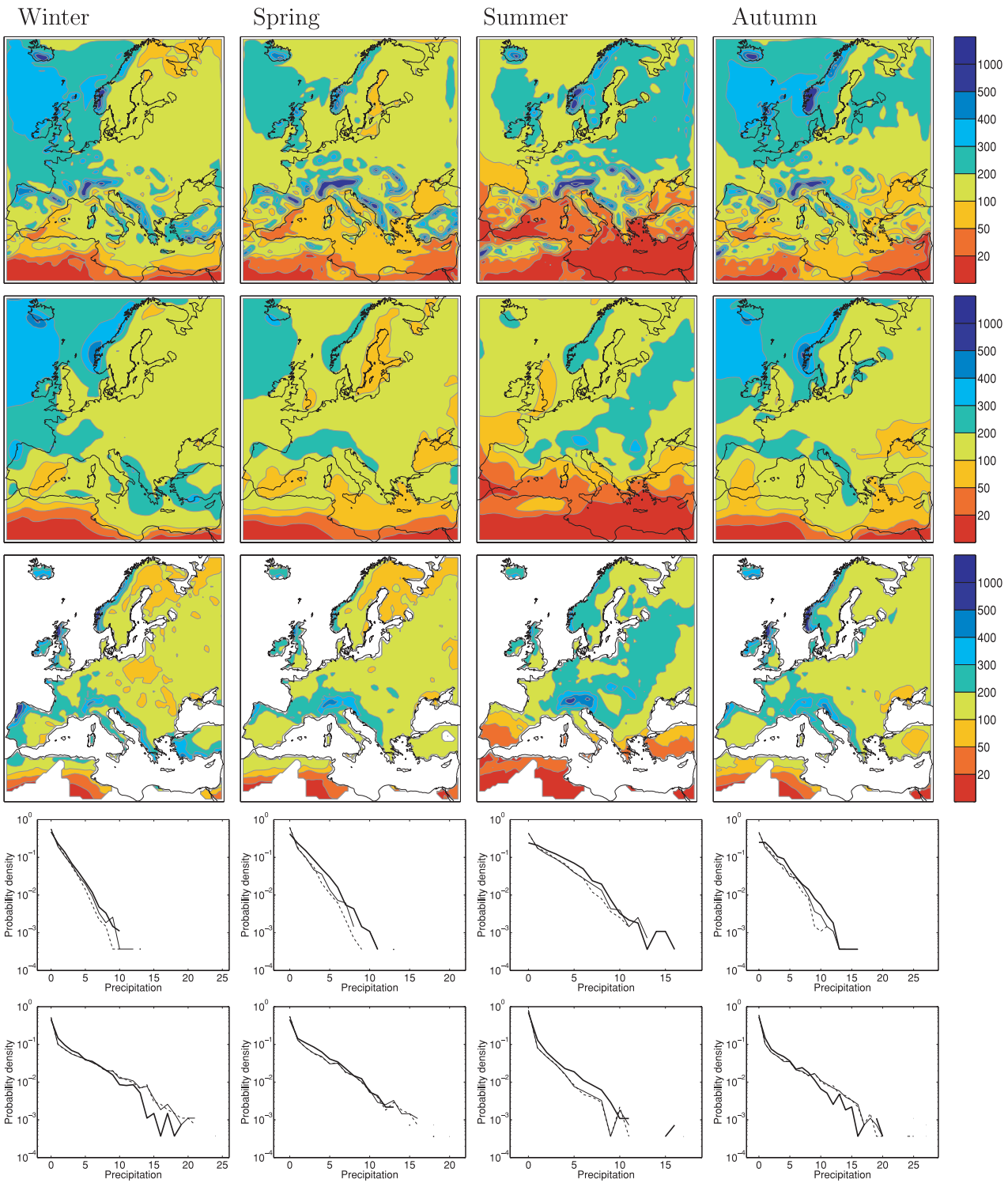

Fig. 6. Maps from top to bottom: Seasonal mean precipitation (mm per 3 months) in RCA3, in ERA40 and for an observed mean value of CRU and E-OBS2 data. PDF top panel: Probability density functions of daily precipitation (mm day^{-1}) for RCA3 (thick) and both versions of E-OBS (thin); version 1 (solid) and version 2 (dashed) for Sweden. PDF bottom panels: As panels above but for the Iberian Peninsula. The columns represent the four seasons winter, spring, summer and autumn.

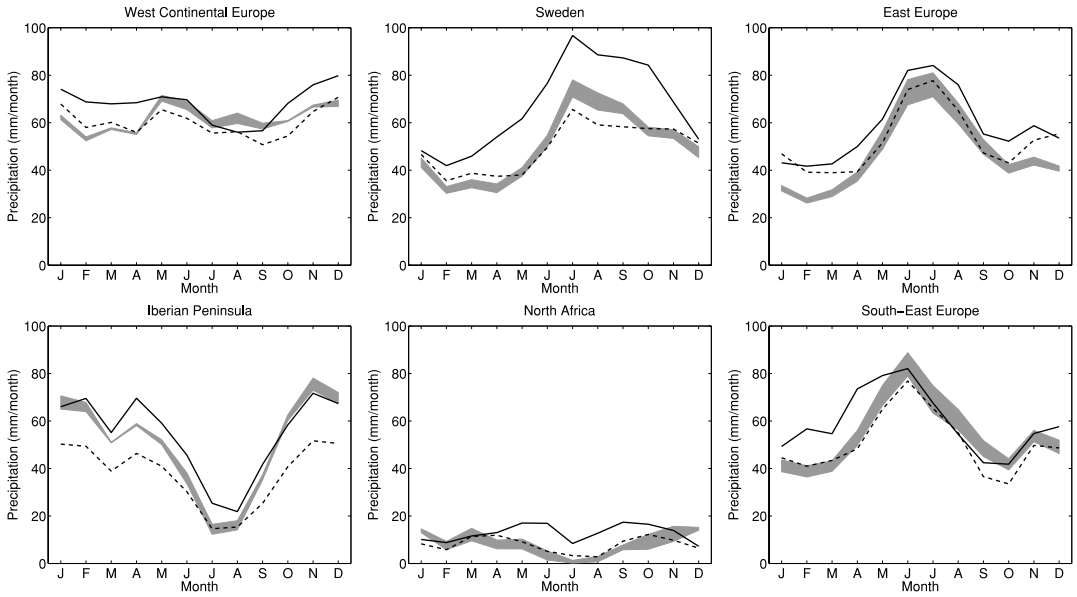

Fig. 7. Seasonal cycle of precipitation over six regions (mm month^{-1}). The line types represent RCA3 (solid) and ERA40 (dashed). The grey-shaded area includes observations based on CRU and E-OBS2.

which, due to its smoother orography, has precipitation extending to the west of Norway over the ocean. The geographical distribution of precipitation over the British Isles is also much better captured in RCA3 compared to ERA40 in all seasons. In all mountainous regions, RCA3 simulates more precipitation than seen in ERA40 and the gridded observations.

The fact that observations are lower may partly be explained by the well-known problem of undercatch of precipitation by rain gauges, which maximizes in regions and periods when snow is the dominant form of precipitation and high wind speeds prevail (Frei et al., 2003). Ungersböck et al. (2001) showed a strong seasonal cycle in the required precipitation correction for the Baltic drainage basin, ranging from +40% in the winter to +10% in summer. They indicate that similar correction numbers are necessary over mid-latitude North America as well. Lind and Kjellström (2009) concluded that RCA3 overestimates precipitation in the Baltic Sea drainage basin by ∼20% compared to the uncorrected CRU observations. However, a shorter but likely more accurate data set by Rubel and Hantel (2001) indicates an overestimate of only 5%. In regions of complex topography, undercatch problems can be further compounded by non-representative gauge distributions and, in low-resolution data sets, by spatial interpolation across steep and localized precipitation gradients (Schwarb et al., 2001). Frei et al. (2003) indicated that undercatch over the Alps varies both by season, ranging from ∼25% in winter to ∼10% in summer, and by altitude, with maximum impact in winter where bias corrections range from 8% for stations below 600 m altitude to corrections as high as 40% above 1500 m. Such uncertainties should be kept in mind when precipitation is evaluated, particularly in regions of complex topography. Even with these caveats in mind, it does appear from Fig. 6 that RCA3 overestimates precipitation, particularly over mountain tops in Scandinavia and the Alps. Such an overestimate may be linked to an overestimate of cloud fraction in these regions. Willén (2008) found the cloud fraction overestimated in RCA3 compared to satellite and surface measurements in mountain areas. Accurately simulating vertical velocities in complex mountainous terrain is known to be difficult in numerical models and may contribute to an erroneous forcing of the grid scale precipitation scheme in RCA3 mountainous areas. A further problem may also be linked to the use of the resolved scale vertical velocity as part of the convective trigger function in the Kain–Fritsch convection scheme, which appears to be associated with excessive convective triggering over mountainous regions during the summer season.

Figure 7 indicates that RCA3 accurately captures the amplitude and phase of the annual cycle of precipitation in most areas of Europe. Overestimated precipitation is suggested in the winter season for West and Eastern Europe and Sweden, although the size of this overestimate is difficult to judge given the aforementioned corrections that are likely required for the observations. Over Sweden, a summer and early autumn overestimate is clearly visible. Despite the higher resolution in RCA3 compared to that used in ERA40 there is no clear overall improvement in area averaged precipitation in all seasons and regions. The improvement lies in the better representation of the geographical details (cf. Fig. 6).

Recent observational studies suggest a trend towards more frequent intense precipitation events over the past few decades. Such trends have been documented for North America (Karl and Knight, 1998), Japan (Iwashima and Yamamoto, 1993) and Northern Italy (Brunetti et al., 2004). Modelling studies suggest

this trend may continue into the future (Nikulin et al., 2011; López-Moreno and Beniston, 2009). To gain confidence in such projections, it is important to establish that models correctly simulate the frequency and intensity distribution of precipitation for the recent observed past. To assess this, Fig. 6 presents PDFs of daily precipitation rates simulated by RCA3 and as described in the two E-OBS data sets. In a gross sense, RCA3 captures quite well the frequency and intensity distribution of precipitation in these two regions and is also able to represent the seasonal evolution of the distributions. A clear overestimate (1–5 mm day^{-1}) of precipitation intensity is seen for Sweden in the spring and summer, with a corresponding underestimate of essentially dry days (precipitation <1 mm day^{-1}). Although a portion of this may be related to observational undercatch, we are confident that the positive bias is real and relates primarily to excess precipitation intensity on the east side (generally lee side) of the Scandinavian mountains. Over Iberia an overestimate of moderate to strong (5–10 mm day^{-1}) events is seen.

4.4. *Clouds and radiation*

In this section, we make a limited evaluation of the RCA3 clouds and surface radiation fluxes, concentrating on systematic biases that impact on the surface temperature. We emphasize the summer season where temperature errors in the diurnal cycle are largest and radiation errors likely maximize. The interested reader is referred to Willén (2008) for a more detailed discussion on the simulated cloud and radiation processes in RCA3.

Figure 8 presents seasonal mean deviations from ERA40 of total cloud cover, downwelling surface SW and LW. We acknowledge potential shortcomings in using these predicted fields from ERA40 as quasi-observations, but note that Markovic et al. (2009) indicate a high level of quality in the ERA40 cloud cover and surface radiation fluxes compared to six surface measurement sites over North America. The relative quality of the ERA40 clouds has also been confirmed for Northern Europe in the study of Willén (2008).

Cloud fraction is set to zero at the outer point of the RCA domain and there is generally a rapid gradient in cloud fraction across the eight-point relaxation zone, cloud fraction errors close to the edge of the domain in Fig. 8 largely represent this feature. Over Europe RCA3 cloud fraction biases in the summer exhibit a dipole pattern, with a positive bias of 5–10% over Northern Europe and a negative bias, of similar magnitude to the south. These biases partly contribute to the surface radiation flux errors shown in Fig. 8. In Southern Europe incoming SW exhibits a positive deviation from ERA40 of 10–30 Wm^{-2}, whereas over Northern Europe a smaller negative deviation can be seen. Comparison to 28 European surface radiation stations in the GEBA network (Gilgen and Ohmura, 1999) indicate RCA3 actually has a somewhat smaller positive bias of ∼5–20 Wm^{-2}, whereas ERA40 values are negatively biased compared to GEBA by ∼5–10 Wm^{-2} (not shown).

Errors in cloud fraction also contribute to surface LW errors, with the positive bias in cloud fraction over Northern Europe spatially collocated with a positive LW bias of 5–15 Wm^{-2}. In terms of total incoming radiation, errors in Northern Europe tend to partly cancel, leading to a relatively accurate summer near-surface temperature in RCA3, when averaged across the diurnal cycle (Fig. 4). The negative SW bias in Fig. 8 has been averaged across the diurnal cycle. In fact, SW errors will occur only during daylight hours and, in an absolute sense, will

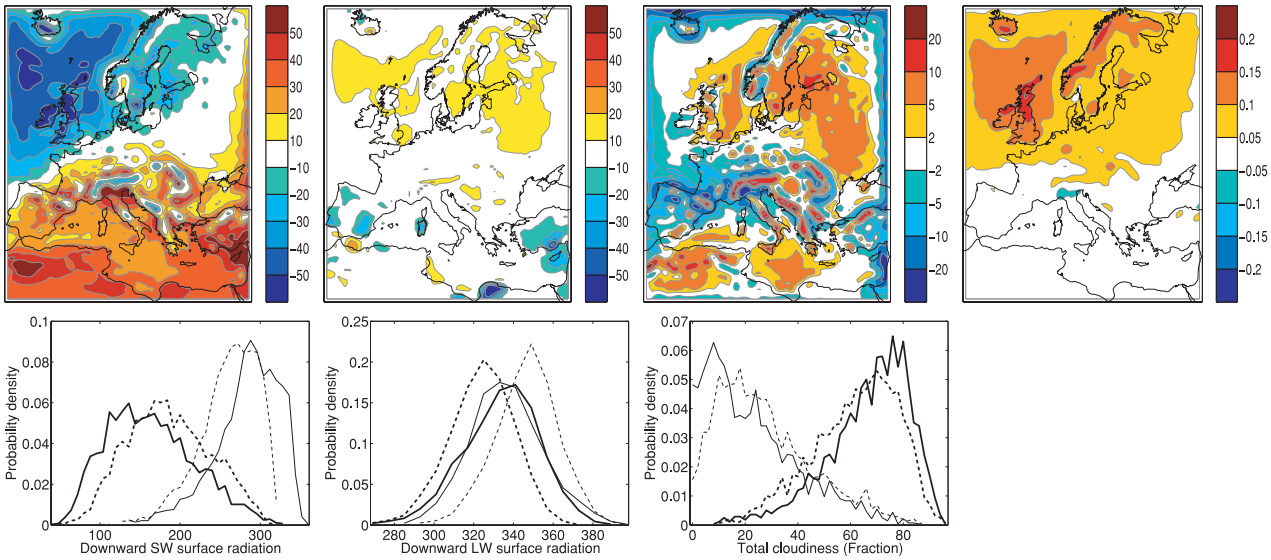

Fig. 8. Top panel: Summer mean difference (RCA3-ERA40) in (from left to right) downward short-wave radiation (Wm^{-2}), downward long-wave radiation (Wm^{-2}), total cloudiness (%) and vertically integrated LWP as seen in the RCA3 radiation code (kg m^{-2}). Bottom panel: Probability density functions of the top panels variables for RCA3 (solid) and ERA40 (dashed) for Sweden (thick) and the Iberian Peninsula (thin).

increase as the incoming solar flux increases to its maximum at local noon. Hence the negative bias in SW over Northern Europe will tend to dominate the surface radiation budget during the local afternoon, partly explaining the large underestimate of maximum summer temperatures shown in Fig. 4. Conversely, at night the positive bias in LW operates in isolation leading to the warm bias in nocturnal minimum temperatures over Northern Europe.

Fractional cover is not the only cloud variable that contributes to errors in cloud reflectivity and emissivity. For a given cloud fraction, total solar reflectivity also depends on the total water content in the cloud, the phase distribution of this water and the dominant droplet/crystal size (Liou, 1992). Many of these parameters are difficult to evaluate due to lack of observations. In Fig. 8 we compare the summer vertically integrated Liquid Water Path (LWP) against the equivalent field from ERA40. The LWP in RCA (and in the ECMWF model) is multiplied by an inhomogeneity factor of 0.7 (Tiedkte, 1996) which gives the radiatively active LWP in the model as shown in Fig. 8. This scaling is done in order to account for observed variability of cloud water in the model radiation schemes. Compared to ERA40, RCA3 has a large positive bias in LWP, with a positive bias over the North Atlantic of more than ∼50%. O'Dell et al. (2008) suggest the ERA40 LWP values are consistent with satellite-based retrievals over mid-latitude oceans. Hence the overestimate in RCA3 seems genuine and is consistent with the negative bias seen in surface SW against ERA40 in this region. Over land areas of Northern Europe LWP biases relative to ERA40 are ∼0.07 mm, or roughly 40–50% higher than the ERA40 values of ∼0.15 mm. Roebling and van Meijgaard (2009) indicate that for summer 2004, SEVIRI satellite retrievals give LWP values in Northern Europe of ∼0.12 mm and that ECMWF forecasts overestimate this by ∼25%, consistent with the climatological estimates quoted above for ERA40. This implies that over North Europe RCA3 actually overestimates LWP by 50–75% relative to satellite observations. Similar results were found by Illingworth et al. (2007) and Willén (2008) in comparing RCA3 LWP with surface based radar and lidar measurements. During winter, RCA3 has a similar positive LWP bias but located over Iberia and France (not shown). This excess LWP and associated SW flux error contributes to the underestimate of maximum temperatures in winter over Iberia (Figs 4 and 5). In the development version of RCA4 this positive cloud water bias has been significantly improved (see Barrett et al., 2009, for a preliminary evaluation of the RCA4 diurnal cycle of clouds) leading to commensurate improvements in the surface radiation fluxes.

PDFs of the daily mean surface SW over Sweden and Iberia (Fig. 8) clearly show the systematic negative and positive biases, respectively, across the SW distribution. Similar shifts are also seen for LW. The simulated PDFs of daily cloud fraction are very accurate, both in the median value as well as the width and shape of the distribution. This is the case both for Sweden, with a peak in the summer distribution of ∼75% in both model and ERA40 and Iberia with an oppositely shaped distribution, peaking at cloud fractions of ∼10%. The main error in the cloud fraction distributions lies in the overestimate of cloud-free days in RCA3 over Iberia, likely linked with too frequent and/or too intense anti-cyclonic conditions indicated in the MSLP PDF of Fig. 3.

4.5. *Surface energy fluxes*

Figure 9 shows the mean annual cycle of upward sensible (H) and latent (LE) heat fluxes, along with the net radiation flux (Rn) for RCA3 and ERA40 averaged over Sweden and the Iberian peninsula. Shortcomings in ERA40 surface energy fluxes compared to observations are discussed below. During the summer, Rn is clearly underestimated over both Sweden and Iberia (Fig. 9). Over Sweden this difference is mainly due to an underestimate of incoming shortwave radiation compared to ERA40 (Fig. 8) whereas over the Iberian Peninsula the excess in incoming SW is compensated by a relatively high surface albedo for open land (0.28), resulting in a more accurate net surface solar radiation budget. The negative bias in Rn therefore primarily reflects an underestimate of downwelling LW radiation over Iberia (Fig. 8).

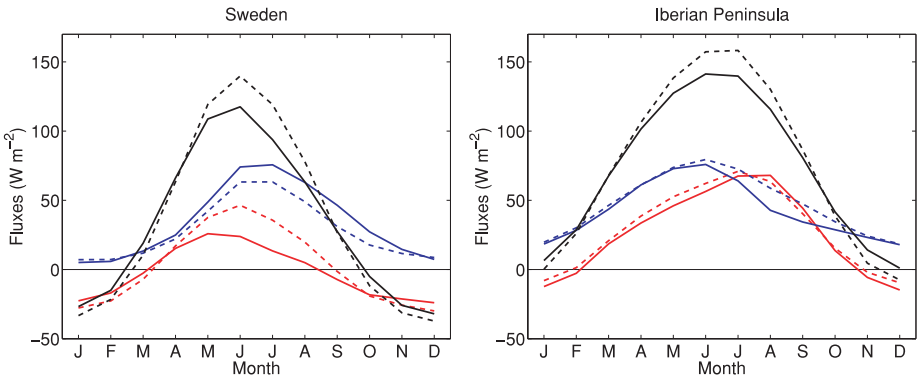

Fig. 9. Annual cycles of net radiation (black, Wm^{-2}), sensible (red, Wm^{-2}) and latent (blue, Wm^{-2}) heat fluxes for RCA3 (solid) and ERA40 (dashed) over Sweden and the Iberian Peninsula.

Although less Rn is available over Sweden in summer compared to ERA40, LE is still larger than in ERA40, compensated by a smaller H. According to Betts et al. (2006) ERA40 overestimates LE over a conifer forest dominated landscape in Canada, a landscape similar to that over Sweden. They speculate on different reasons for this overestimate, e.g. that surface conductance may be too high, evaporation of intercepted water may be overestimated or that vertical exchange processes between the surface and atmosphere may be too efficient. In RCA3, the parametric description of these processes are somewhat similar to the ECMWF LSS employed in ERA40. A corresponding overestimate of LE may therefore also be expected. However, RCA3 exhibits a positive bias in LE even compared to ERA40. This bias is clearly correlated with a positive bias in precipitation over the same region (Fig. 7), which through its impact on soil moisture can cause or amplify an LE bias. Because the surface and atmospheric water cycles are tightly coupled it is difficult to identify the underlying cause of these errors over Sweden. To understand this further, we are presently running the RCA3 LSS offline, forced by observed atmospheric input over a number of European sites and comparing results directly with observed surface fluxes.

Over the Iberian Peninsula, H and LE in RCA3 generally corresponds well with ERA40, although with a slightly less LE in RCA3 during summer-autumn. The simulated summer Bowen Ratio (BR = H/LE) in RCA3 for Southern Europe is in the range 1–2 (not shown) which at least corresponds well with observations reported by Jaeger et al. (2009) where summer BR for an Italian site was in the range 1.5–2 for a 4 years period.

4.6. Snow

The relatively coarse horizontal resolution of ERA40, and consequently smooth orography, acts to distribute snow more smoothly than the higher resolution in RCA3 (Fig. 10). This effect is most obvious in the west–east gradient of the water content of the snow, the snow-water equivalent (SWE), across Scandinavia, where RCA3 produces much higher SWE values in the Norwegian and Swedish mountains than east of the mountains. In Fig. 10, we compare the RCA3 SWE against point observations made at a number of SYNOP stations in Sweden. Generally the RCA3 SWE values correspond well with observations, particularly in Southern and Central Sweden. In Northern Sweden, close to the mountains (the three left most groups of bars in Fig. 10), the agreement is worse, although averaging model and observed values across these three stations indicates that the RCA3 SWE vales are quite accurate even in mountainous regions. The individual differences at these sites likely arise due to detailed aspects of topography and snow amounts that are not possible for RCA3 to resolve at a 50 km resolution. Over Finland and Northwest Russia RCA3 underestimates SWE compared to ERA40. A study by Drusch et al. (2004) that introduced a revision into the ECMWF snow analysis scheme suggests that the system used in the ERA40 process may overestimate SWE over large parts of Eurasia. This, along with the good agreement of RCA3 SWE over Sweden and the implied overestimate in this region of the ERA40 SWE values, makes us cautious with regard to an SWE bias calculated in relation to ERA40.

In Kjellström et al. (2005), snow cover duration was also evaluated with RCA3 producing quite accurate results in comparison to a time-limited climatology over Sweden.

4.7. Wind

The 10 m wind-speed climate in RCA3 has been thoroughly evaluated over North America in a study by He et al. (2010). RCA3 winds were compared to two other RCM simulations and to both the ERA40 and NCEP reanalyses, generally outperforming all these data sets. They conclude that RCA3 is able to capture both the correct seasonality of the 10 m wind speed and its sensitivity to land-surface type (open land, forest, water). However, median wind speeds are generally underestimated and, for water-dominated regions, the high wind-speed end of the distribution is underestimated. In their study they conclude that care must be taken in comparing gridbox-average wind speeds directly with station observations in regions of strong surface heterogeneity. They show that the PDF of simulated night-time 10 m wind speed over open land is closer to observations than the corresponding PDF based on grid-averaged values.

A diagnostic gustiness parameterization based on Brasseur (2001) has been implemented in RCA3 by Nordström (2005). An evaluation of simulated gust wind-speeds against analysed observations (Häggmark et al., 2000) over Sweden gives quite satisfactory results for both the maximum daily gusts and for the maximum monthly gusts with most differences in seasonal mean values during winter being within ± 1 m s^{-1} (Kjellström et al., 2005). However, the original Brasseur method gave an overestimation of simulated gust wind-speeds over land. A modification was therefore introduced into RCA3 to reduce this bias. The modification utilizes information on local surface roughness length over land and has been tuned against Swedish station data. The resulting gust wind speeds have yet to be evaluated for other regions.

5. Discussion and conclusion

In this paper, we provide a general description of the physics in RCA3, with particular reference to modifications compared to the previous full release, RCA2. The model performance is evaluated over Europe for the recent past climate, with an emphasis on near-surface variables of interest to researchers using RCA3 results in climate impact studies. For many variables, RCA3 represents the European climate well when compared to other RCMs (Hagemann et al., 2004). However, systematic biases do still exist. In general RCA3 shows equally good, or

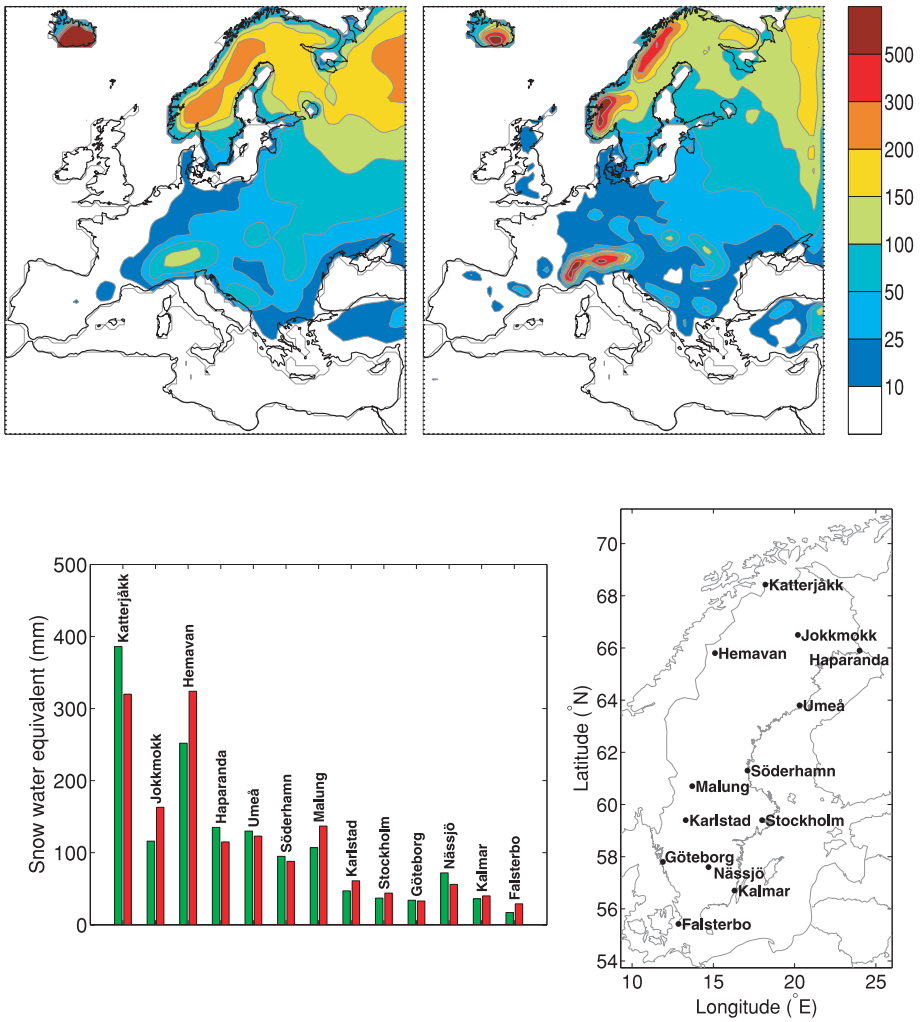

Fig. 10. Top panel: The average yearly maximum water content (mm) 1961–1990 of the snow pack according to ERA40 (left) and RCA3 (right), respectively. Bottom panel: Average annual maximum snow water content (mm) 1968–1993 (left) at selected Swedish sites (right) from RCA3 (red) and from observations (green) (Raab and Vedin, 1995).

better, correspondence to observations than earlier model versions (Kjellström et al., 2005), while now being physically more realistic in terms of the underlying processes described in the model. Results discussed in this paper are from a 50 km version of the model, the main conclusions regarding model quality and biases over Europe generally also hold for 25 km resolution.

The major change in RCA3 compared to RCA2 was the introduction of a tiled surface scheme. It was recognized that only one surface temperature representing all kinds of different surfaces in RCA2 (snow, forest, grass, ice) was not sufficient for capturing the range of possible feedbacks associated with future climate change. In RCA3 different subsurfaces, tiles, in a grid box are represented by individual temperatures and surface energy balance calculations. The concept of double-energy balance was introduced for the forest tile which means that the canopy and the forest floor are given separate energy balances and temperatures. Along with these changes in the surface scheme, a range of smaller updates were also made in the atmospheric physics related to the radiation, turbulence and cloud parameterizations.

On a seasonal basis, the mean temperature errors are generally within $\pm 1^{\circ}$C except during winter, when a positive bias is found in the north-eastern part of the model domain and a negative bias over the Mediterranean. Although, the overall mean temperature climate is satisfactory, there remain some discrepancies in internal model parameters as well as simulated quantities with respect to observations. For example, a too high albedo for snow free open land balances an excess incoming solar radiation in Southern Europe. In Northern Europe, an underestimated SW radiation flux and an overestimated LW flux drive different signed temperature errors by night and day that tend to cancel out when averaged across diurnal cycle. In Northern Europe there is a clear

underestimate in maximum temperatures and an overestimate in minimum temperatures. Two of the likely causes of these errors were discussed in Section 4.2.2, namely; a positive bias in cloud water and an overestimate of soil heat flux. With results from the development version of RCA4 it was shown that the main reason for the underestimated diurnal cycle over Sweden is related to the overestimated soil heat flux. The soil heat flux was reduced by the introduction of an organic carbon component in the soil as recommended by Lawrence and Slater (2008), which led to an improved diurnal temperature range.

Generally, the seasonal cycle of precipitation is well captured across Europe, apart from a clear overestimate in Northern Europe during summer. This bias is closely linked with an overestimate of surface evaporation over Sweden in summer. Further work is required to determine cause and effect with respect to these coupled errors in precipitation and surface evaporation. In terms of the intensity distribution of precipitation, the model reproduces the observed variability quite well, apart from an overestimate in weak to moderate precipitation over Sweden during spring and summer and an overestimate of moderate to strong events over Iberia in summer. As a result of the relatively accurate precipitation climatology, simulated snow water amounts were found to be quite realistic. Further evaluation of precipitation will concentrate on the benefits accruing from resolution increases beyond 25 km, where possible using high-resolution observations corrected for precipitation undercatch.

Some of the systematic biases in near-surface temperature have been linked to problems in representing cloud and radiation processes in RCA3. The overestimate of cloud water in the model contributes to an underestimate of temperature maxima in summer over Northern Europe and to an underestimate during winter over Southern Europe. These problems have been mitigated somewhat in the latest version of RCA4, where the cloud water excess is improved significantly (Barrett et al. 2009) leading to commensurate improvements in the surface radiation fluxes. The main changes between RCA3 and RCA4, leading to these improvements are a combination of; (i) modifying the TKE mixing scheme to be phrased in moist thermodynamic variables, liquid water potential temperature, (θ_l) and total water (q_t), thereby allowing moist processes to be included in the calculation of TKE, (ii) including a parameterization of cloud top entrainment within the new moist TKE scheme and (iii) modifying the autoconversion calculation for precipitation onset in the RCA large-scale condensation scheme. A more detailed evaluation of these and other model improvements are deferred until the full release of RCA4.

The intention of this paper has been to describe the physical parameterizations in RCA3 and document the main strengths and weaknesses of the model when simulating climate processes over Europe. Knowledge of such systematic biases is important when the model is applied to simulate future climate conditions and when output subsequently is used in the range of climate impact studies.

6. Acknowledgments

The model simulations were made on the climate computing resource Tornado funded with a grant from the Knut and Alice Wallenberg foundation and housed at the National Supercomputing Centre at Linköping University. Part of the analysis work has been funded by the Swedish Mistra-SWECIA programme funded by Mistra (the Foundation for Strategic Environmental Research).

References

Albrecht, B. A. 1981. Parameterization of trade-cumulus cloud amounts. *J. Atmos. Sci.* **38**, 97–105.

Barker, H. W. 1996. A parameterization for computing grid-averaged solar fluxes for inhomogeneous marine boundary layer clouds. Part I: Methodology and Homogeneous Biases. *J. Atmos. Sci.* **53**, 2289–2303.

Barker, H. W., Wielicki, B. A. and Parker, L. 1996. A parameterization for computing grid-averaged solar fluxes for inhomogeneous marine boundary layer clouds. Part II: Validation using satellite data. *J. Atmos. Sci.* **53**, 2304–23216.

Barker, H. W. and Wielicki, B. A. 1997. Parameterizing grid-averaged longwave fluxes for inhomogeneous marine boundary layer clouds. *J. Atmos. Sci.* **54**, 2785–2798.

Barrett, A. I., Hogan, R. J. and O'Connor, E. J. 2009. Evaluating forecasts of the evolution of the cloudy boundary layer using diurnal composites of radar and lidar observations. *Geophys. Res. Lett.* **36**, L17811, doi:10.1029/2009GL038919.

Betts, A. K., Ball, J. H., Barr, A. G., Black, T. A., McCaughey, J. H. and co-authors 2006. Assessing land-surface-atmosphere coupling in the ERA-40 reanalysis with boreal forest data. *Agric. Forest Meteorol.* **140**, 365–382.

Brasseur, O. 2001. Development and application of a physical approach to estimating wind gusts, *Monthly Weather Rev.* **129**, 5–25.

Bringfelt, B., Räisänen, J., Gollvik, S., Lindström, G., Graham, L. P. and co-authors. 2001. The land surface treatment for the Rossby Centre regional atmosphere climate model – version 2, Reports of Meteorology and Climatology 98, SMHI, SE-601 76 Norrköping, Sweden.

Brinkop, S. and Roeckner, E. 1995. Sensitivity of a general circulation model to parameterizations of cloud-turbulence interactions in the atmospheric boundary layer. *Tellus* **47A**, 197–220.

Brunetti, M., Buffoni, L., Mangianti, F., Maugeri, M. and Nanni, T. 2004. Temperature, precipitation and extreme events during the last century in Italy. *Global Planet. Change* **40**, 141–149.

Cahalan, R. F., Ridgeway, W., Wiscombe, W. J., Bell, T. L. and Snider, J. B. 1994. The albedo of fractal clouds. *J. Atmos. Sci.* **51**, 2434–2455.

Choudhury, B. J. and Monteith, J. L. 1988. A four-layer model for the heat budget of homogeneous land surfaces. *Q. J. R. Meteorol. Soc.* **114**, 373–398.

Clapp, R. B. and Hornberger, G. M. 1978. Empirical equations for some soil hydraulic properties. *Water Resources Res.* **14**, 601–604.

Cuijpers, J. W. M. and Duynkerke, P. G. 1993. Large eddy simulations of trade wind with cumulus clouds. *J. Atmos. Sci.* **50**, 3894–3908.

Cuxart, J., Bougeault, P. and Redelsperger, J.-L. 2000. A turbulence scheme allowing for mesoscale and large-eddy simulations. *Q. J. R. Meteorol. Soc.* **126**, 1–30.

Davies, H. C. 1976. A lateral boundary formulation for multi-level prediction models. *Q. J. R. Meteorol. Soc.* **102**, 405–418.

Deardorff, J. W. 1978. Efficient prediction of ground surface temperature and moisture, with inclusion of a layer of vegetation. *J. Geophys. Res.* **83**, 1889–1903.

Douville, H., Royer, J.-F. and Mahfouf, J.-F. 1995. A new snow parameterization for the Météo-France climate model. Part I: Validation in stand-alone experiments. *Clim. Dyn.* **12**, 21–35.

Döscher, R., Wyser, K., Meier, H. E. M., Qian, M. and Redler, R. 2009. Quantifying Arctic contributions to climate predictability in a regional coupled ocean-ice-atmosphere model. *Clim. Dyn.* **34**, doi: 10.1007/s00382-009-0567-y.

Drusch, M., Vasiljevic, D. and Viterbo, P. 2004. ECMWF's global snow analysis: assessment and revision based on satellite observations. *J. Appl. Meteor.* **43**, 1282–1294.

FAO-UNESCO (ed.), 1981. *Soil Map of the World*, Volume 5. UNESCO-Paris, Europe.

Frei, C., Christensen, J., Dequé, M., Jacob, D. and Vidale, P. 2003. Daily precipitation statistics in regional climate models: evaluation and intercomparison for the European Alps. *J. Geophys. Res.* **108**, 4124–4142.

Gilgen, H. and Ohmura, A. 1999. The Global Energy Balance Archive (GEBA). *Bull. Am. Meteorol. Soc.* **80**, 831–850.

Graham, L. P. 2002. A simple runoff routing routine for the Rossby Centre Regional Climate Model. In: *Proceedings from the XXII Nordic Hydrological Conference* (ed. Killingtveit, A.). Røros, Norway, 4–7 August, 573–580.

Hagemann, S., Botzet, M., Dümenil, L. and Machenhauer, B. 1999. Derivation of global GCM boundary conditions from 1 km land use satellite data. Tech. Rep. 289, Max-Planck-Institute for Meteorology, Hamburg, Germany.

Hagemann S., Machenhauer B., Jones R., Christensen O. B., Déqué M. and co-authors. 2004. Evaluation of water and energy budgets in regional climate models applied over Europe. *Clim. Dyn.* **23**. 547–567.

Häggmark, L., Ivarsson, K.-I., Gollvik, S. and Olofsson, P.-O. 2000. Mesan, an operational mesoscale analysis system. *Tellus* **52A**, 2–20.

Haylock, M. R., Hofstra, N., Klein Tank, A. M. G., Klok, E. J., Jones, P. D. and co-authors. 2008. European daily high-resolution gridded data set of surface temperature and precipitation for 1950–2006. *J. Geophys. Res.* **113**, D20119, doi:10.1029/2008JD010201.

He, Y., Monahan, A. H., Jones, C. G., Dai, A., Biner, S. and co-authors. 2010. Probability distributions of land surface wind speeds over North America, *J. Geophys. Res.* **115**, D04103, doi:10.1029/2008JD010708.

Hillel, D. 1980. *Fundamentals of Soil Physics*. Academic Press, New York.

Illingworth, A. J., Hogan, R. J., O'Connor, E. J., Bouniol, D., Brooks, M. E. and co-authors. 2007. Cloudnet – continuous evaluation of cloud profiles in seven operational models using ground-based observations. *Bull. Am. Meteorol. Soc.* **88**, 883–898.

Iwashima, T. and Yamamoto, R. 1993. A statistical analysis of the extreme events: long term trend of heavy daily precipitation, *J. Meteor. Soc. Jpn.* **71**, 637–640.

Jaeger, E. B., Stöckli, R. and Seneviratne, S. I. 2009. Analysis of planetary boundary layer fluxes and land-atmosphere coupling in the regional climate model CLM. *J. Geophys. Res.* **114**, D17106, doi:10.1029/2008JD011658.

Jarvis, P. G. 1976. The interpretation of the variations in leaf water potential and stomatal conductance found in canopies in the field. *Philos. Trans. R. Soc. Lond.* **B273**, 593–610.

Jones, C. G. and Sanchez, E. 2002. The representation of shallow cumulus convection and associated cloud fields in the Rossby Centre atmospheric model, *HIRLAM Newsletter 41*, SMHI, SE-601 76 Norrköping, Sweden.

Jones, C. G., Samuelsson, P. and Kjellström, E. 2011. Regional climate modelling at Rossby Centre. Preface to the RCA3 special issue in Tellus 63A, 1–3.

Jones, C., Willén, U., Ullerstig, A. and Hansson, U. 2004. The Rossby Centre regional atmospheric climate model part I: model climatology and performance for the present climate over Europe. *Ambio* **33**(4–5), 199–210.

Kain, J. S. 2004. The Kain–Fritsch convective parameterization: an update. *J. Appl. Meteorl.* **43**, 170–181.

Kain, J. S. and Fritsch, J. M. 1990. A one-dimensional entraining/detraining plume model and its application in convective parameterization. *J. Atmos. Sci.* **47**, 2784–2802.

Kain, J. S. and Fritsch, J. M. 1993. Convective parameterizations for mesoscale models: The Kain–Fritsch scheme. In: *The Representation of Cumulus Convection in Numerical Models* (eds. Emanuel, K. A. and Raymond, D. J.). American Meteorological Society Monograph, Boston, USA, 246 pp.

Källén, E. (ed.). 1996. *HIRLAM Documentation Manual. System 2.5*. Available on request from SMHI, SE-60176 Norrköping, Sweden.

Karl, T. R. and Knight, R. W. 1998. Secular trends of precipitation amount, frequency, and intensity in the United States. *Bull. Am. Meteorl. Soc.* **79**, 231–241.

Kjellström E., Bärring L., Gollvik S., Hansson U., Jones C. and co-authors. 2005. A 140-year simulation of European climate with the new version of the Rossby Centre regional atmospheric climate model (RCA3). Report in Meteorology and Climatology 108, SMHI, SE-60176 Norrköping, Sweden, 54 pp.

Kjellström, E., Bärring, L., Jacob, D., Jones, R., Lenderink, G. and co-authors. 2007. Variability in daily maximum and minimum temperatures: recent and future changes over Europe. *Clim. Change* **81**, 249–265, doi:10.1007/s10584-006-9220-5.

Koster, R. D. and Suarez, M. J. 1992. A comparative analysis of two land-surface heterogeneity representations. *J. Climate* **5**, 1379–1390.

Lawrence D. M. and Slater A. G. 2008. Incorporating organic soil into a global climate model. *Clim. Dyn.* **30**, 145–160.

Lenderink, G. and de Rooy, W. 2000. A robust mixing length formulation for a TKE-1 turbulence scheme, *HIRLAM Newsletter 36*, KNMI, The Netherlands, 25–29.

Lenderink, G. and Holtslag, A. A. M. 2004. An updated length-scale formulation for turbulent mixing in clear and cloudy boundary layers. *Q. J. R. Meteorol. Soc.* **130**, 3405–3427.

Lind, P. and Kjellström, E. 2009. Water budget in the Baltic Sea drainage basin: evaluation of simulated fluxes in a regional climate model. *Boreal Environ. Res.* **14**, 56–67.

Lindström, G. and Gardelin, M. 1999. A simple snow parameterization scheme intended for the RCA model based on the HBV runoff model. *SWECLIM Newsletter 6*, SMHI, Sweden, 16–20.

Lindström, G., Johansson, B., Persson, M., Gardelin, M. and Bergström, S. 1997. Development and test of the distributed HBV-96 hydrological model. *J. Hydrol.* **201**, 272–288.

Liou, K.-N. 1992. *Radiation and Cloud Processes in the Atmosphere: Theory, Observation, and Modeling*. Oxford University Press, Oxford, UK.

Ljungemyr, P., Gustafsson, N. and Omstedt, A. 1996. Parameterization of lake thermodynamics in a high-resolution weather forecasting model. *Tellus* **48A**, 608–621.

López-Moreno, J. I. and Beniston, M. 2009. Daily intensity precipitation for the 21st century: seasonal changes over an Atlantic-Mediterranean gradient in the Pyrenean mountains. *Theor. Appl. Climatol.* **95**, 375–384.

Louis, J. F., Tiedtke, M. and Geleyn, J. F. 1982. A short history of the PBL parameterization at ECMWF. In: *Workshop on Boundary Layer Parameterization*, European Centre for Medium-Range Weather Forecasts Reading, UK, 59–79.

Lucas-Picher, P., Caya, D., de Elia, R. and Laprise, R. 2008. Investigation of regional climate models' internal variability with a ten-member ensemble of ten-year simulations over a large domain. *Clim. Dyn.* **31**, 927–940. doi:10.1007/s00382-008-0384-8

Markovic, M., Jones, C. G., Wingera, K. and Paquinb, D. 2009. The surface radiation budget over North America: gridded data assessment and evaluation of regional climate models. *Int. J. Climatol.* **29**, 2226–2240.

Masson V., Champeaux J. L., Chauvin F., Mériguet C. and Lacaze R. 2003. A global database of land surface parameters at 1km resolution for use in meteorological and climate models. *J. Climate* **16**.1261–1282.

McCumber, M. C. and Pielke, R. A. 1981. Simulation of the effects of surface fluxes of heat and moisture in a mesoscale numerical model 1. Soil layer. *J. Geophys. Res*. 86, 9929–9938.

Milton, S. and Wilson, C. 1996. The impact of parameterized subgrid-scale orographic forcing on systematic errors in a global NWP model. *Mon. Wea. Rev*. 124, 2023–2045.

Mitchell, T. D. and Jones, P. D. 2005. An improved method of constructing a database of monthly climate observations and associated high-resolution grids. *Int. J. Climatol.* **25**, 693–712.

Nikulin, G., Kjellström, E., Hansson, U., Strandberg, G. and Ullerstig, A. 2011. Evaluation and future projections of temperature, precipitation and wind extremes over europe in an ensemble of regional climate simulations. *Tellus* **63A**, 41–55.

Noilhan, J. and Planton, S. 1989. A simple parameterization of land surface processes for meteorological models. *Mon. Wea. Rev.* **117**, 536–549.

Nordström, M. 2005. Estimation of gusty winds in RCA. *Master thesis*, Department of Earth Sciences, Uppsala University. ISSN 1650-6553 Nr 101. 42 pp.

O'Dell, C. W., Wentz, F. J. and Bennartz, R. 2008. Cloud liquid water path from satellite-based passive microwave observations: a new climatology over the global oceans. *J. Clim.* **21**, 1721–1739.

Raab, B. and Vedin, H., Eds., 1995. *Climate, Lakes and Rivers. National Atlas of Sweden*, Vol. 14. SNA Publishing, Box 45029 SE-10430 Stockholm, Sweden, 176 pp.

Räisänen, J., Hansson, U., Ullerstig, A., Döscher, R., Graham, L. P. and co-authors. 2003. GCM driven simulations of recent and future climate with the Rossby Centre coupled atmosphere – Baltic Sea regional climate model RCAO, Reports Meteorology and Climatology 101, SMHI, SE-601 76 Norrköping, Sweden.

Räisänen, P., Rummukainen, M. and Räisänen, J. 2000. Modification of the HIRLAM radiation scheme for use in the Rossby Centre regional atmospheric climate model, Reports Meteorology and Climatology 49, Department of Meteorology, University of Helsinki, Finland.

Rasch, P. J. and Kristjánsson, J. E. 1998. A comparison of the CCM3 model climate using diagnosed and predicted condensate parameterizations. *J. Climate* **11**, 1587–1614.

Roebeling, R. A. and van Meijgaard, E. 2009. Evaluation of the daylight cycle of model predicted cloud amount and condensed water path over Europe with observations from MSG-SEVIRI. *J. Climate* **22**, 1749–1766. doi: 10.1175/2008JCLI2391.1.

Rubel, F. and Hantel, M. 2001. BALTEX 1/6-degree daily precipitation climatology. *Meteorol. Atmos. Phys.* **77**. 155–166.

Rummukainen, M. 2010. State-of-the-art with regional climate models. *WIREs Climate Change* 1, 82–96, doi: 10.1002/wcc.008.

Samuelsson P., Gollvik S. and Ullerstig A. 2006. The land-surface scheme of the Rossby Centre regional atmospheric climate model (RCA3). Report in Meteorology 122. SMHI, SE-60176 Norrköping, Sweden, 25 pp.

Sass B. H., Rontu L., Savijärvi H. and Räisänen P. 1994. HIRLAM-2 Radiation scheme: documentation and tests. Hirlam Technical Report No. 16, SMHI, SE-60176 Norrköping, Sweden, 43 pp.

Savijärvi H. 1990. A fast radiation scheme for mesoscale model and short-range forecast models. *J. Appl. Met.* **29**. 437–447.

Schwarb, M., Daly, C., Frei, C. and Schär, C. 2001. Mean seasonal precipitation throughout the European Alps, 1971–1990. Hydrologic Atlas of Switzerland, National Hydrologic Service, Bern.

Sellers, P. J., Dickinson, R. E., Randall, D. A., Betts, A. K., Hall, F. G. and co-authors. 1997. Modeling the exchanges of energy, water, and carbon between continents and the atmosphere. *Science* **275**, 502–509, doi: 10.1126/science.275.5299.502.

Shuttleworth, W. J. and Wallace, J. S. 1985. Evaporation from sparse crops-an energy combination theory. *Q. J. R. Meteorol. Soc.* **111**, 839–855.

Simmons, A. J. and Burridge, D. M. 1981. An energy and angular-momentum conserving finite-difference scheme and hybrid vertical coordinates. *Mon. Wea. Rev.* **109**, 758–766.

Slingo, A. and Schrecker, H. M. 1982. On the shortwave radiative properties of stratiform water clouds. *Q. J. R. Meteorol. Soc.* **108**, 407–426.

Smith S. A., Doyle, J. D., Brown, A. R., Webster, S. 2006. Sensitivity of resolved mountain drag to model resolution for MAP case-studies. *Q. J. R. Meteorol. Soc.* **132**, 1467–1487.

Stephens, G. L. and Webster, P. J. 1979. Sensitivity of radiative forcing to variable cloud and moisture. *J. Atmos. Sci.* **36**, 1542–1556.

Tiedtke, M. 1996. An extension of cloud-radiation parameterization in the ECMWF model: the representation of subgrid-scale variations of optical depth. *Mon. Wea. Rev.* **124**, 745–750.

Undén, P., Rontu, L., Järvinen, H., Lynch, P., Calvo, J. and co-authors. 2002. HIRLAM-5 scientific documentation. HIRLAM Report, SMHI, SE-601 76 Norrköping, Sweden, 144 p.

Ungersböck, M., Rubel, F., Fuchs, T. and Rudolf, B. 2001. Bias correction of global daily rain gauge measurements. *Phys. Chem. Earth (B)* **26**, 411–414.

Uppala, S. M., Kållberg, P. W., Simmons, A. J., Andrae, U., da Costa Bechtold, V. and co-authors. 2005. The ERA-40 Re-analysis. *Q. J. R. Meteorol. Soc.* **131**, 2961–3012.

Van Den Hurk, B. J. J. M., Viterbo, P., Beljaars, A. C. M. and Betts, A. K. 2000. Offline validation of the ERA40 surface scheme. Technical Memorandum 295, ECMWF, 42 pp.

Van Der Linden, P. and Mitchell, J. F. B. (eds) 2009. ENSEMBLES: Climate Change and its Impacts: Summary of Research and Results from the ENSEMBLES Project. Met Office Hadley Centre, Fitzroy Road, Exeter EX1 3PB, UK, 160 pp.

Viterbo, P., Beljaars, A. and Teixeira, J. 1999. The representation of soil moisture freezing and its impact on the stable boundary layer. *Q. J. R. Meteorol. Soc.* **125**, 2401–2426.

Wallace, J. S., Roberts, J. M. and Sivakumar, M. V. K. 1990. The estimation of transpiration from sparse dryland millet using stomatal conductance and vegetation area indices. *Agric. For. Met.* **51**, 35–49.

Willén, U. 2008. Preliminary use of CM-SAF cloud and radiation products for evaluation of regional climate simulations. Reports Meteorology and Climatology 131, SMHI, SE-601 76 Norrköping, Sweden.

Willmott, C. J. and Matsuura, K. 1995. Smart interpolation of annually averaged air temperature in the United States. *J. Appl. Met.* **34**, 2577–2586.

Wyser, K., Rontu, L. and Savijärvi, H. 1999. Introducing the effective radius into a fast radiation scheme of a mesoscale model. *Contr. Atmos. Phys.* **72**, 205–218.